Check for updates

Joint iterative reconstruction and 3D rigid alignment for X-ray tomography

K. PANDE,[1,2,*] J. J. DONATELLI,[2,3] D. Y. PARKINSON,[4] H. YAN,[5] AND J. A. SETHIAN[2,3,6]

[1]*Molecular Biophysics and Integrated Bio-Imaging Division, Lawrence Berkeley National Laboratory, Berkeley, CA 94720, USA*
[2]*Center for Advanced Mathematics for Energy Research Applications, Lawrence Berkeley National Laboratory, Berkeley, CA 94720, USA*
[3]*Department of Mathematics, Applied Mathematics and Computational Research Division, Lawrence Berkeley National Laboratory, Berkeley, CA 94720, USA*
[4]*Advanced Light Source, Lawrence Berkeley National Laboratory, Berkeley, CA 94720, USA*
[5]*National Synchrotron Light Source II, Brookhaven National Laboratory, Upton, NY 11973, USA*
[6]*Department of Mathematics, University of California, Berkeley, CA 94720, USA*
[*]*kpande@lbl.gov*

Abstract: X-ray tomography is widely used for three-dimensional structure determination in many areas of science, from the millimeter to the nanometer scale. The resolution and quality of the 3D reconstruction is limited by the availability of alignment parameters that correct for the mechanical shifts of the sample or sample stage for the images that constitute a scan. In this paper we describe an algorithm for marker-free, fully automated and accurately aligned and reconstructed X-ray tomography data. Our approach solves the tomographic reconstruction jointly with projection data alignment based on a rigid-body deformation model. We demonstrate the robustness of our method on both synthetic phantom and experimental data and show that our method is highly efficient in recovering relatively large alignment errors without prior knowledge of a low resolution approximation of the 3D structure or a reasonable estimate of alignment parameters.

1.   Introduction

X-ray tomography is a non-destructive technique to image the three-dimensional (3D) structure of a wide variety of materials [1–3]. The technique relies on solving an inverse problem to reconstruct the 3D volume of an unknown object from its two-dimensional (2D) projections as the object is rotated about one or more axes. A fundamental underlying assumption in the reconstruction process is that the relationship between the measured projections and the paths of the X-rays intersecting the object are known exactly, and that there are no unaccounted for additional motions of the object. For nano-scale tomography, however, the projections may be misaligned due to imperfections in the rotation stage or drifts in the illuminating radiations, which if left uncorrected introduce reconstruction artifacts and lead to a loss in resolution. For tomography at longer length scales, there can be other sources of misalignment–such as temperature drifts–especially for longer scans.

A number of approaches have been proposed to align projections in both X-ray and electron tomography. These methods can be roughly classified into two classes: (i) methods based on tracking fiducial markers and features, and (ii) automated, markerless alignment methods. The marker-based methods involve tracking the path of markers such as small gold beads or silica spheres [4–6] that are either mounted on a sample's container (e.g. a capillary) or directly in or on the sample. While highly accurate, fiducial-based methods suffer from the cost of more complicated sample preparation and introduce extra density due to the markers in the 3D

reconstruction that need to be removed for characterizing the sample, and in many cases require significant human time and effort to manually identify the positions of each fiducial on each 2D image. Feature tracking methods employ regions of high contrast in the projections as markers that are identified by various feature detection techniques. The applicability of these methods is limited to cases where a given feature is visible in a range of projections, and even then, the overlap of a large number of features makes the method challenging.

The most common markerless approach for projection alignment is based on the use of cross-correlation between projections acquired at two consecutive rotation angles [7–9] or correlation of the center-of-mass of the sample [10]. The method is successful in determining accurate shot-to-shot jitter, but leads to an overall accumulation of errors resulting in poor alignment of the common axis of rotation. Over the past few decades a new class of alignment algorithms, called projection matching or iterative re-projection, has been introduced [11,12]. These methods aim to simultaneously align the projections and reconstruct the unknown 3D object, and are based on minimizing the inconsistencies between the measured 2D projections with the systematically generated projections from the current guess of the reconstruction. The comparison of the measured (data) and calculated (model) projections can be implemented via cross-correlation of re-projected and measured images [13–15] or minimization of a cost function by quasi-Newton [16] or Levenberg-Marquardt [17,18] schemes. The method in [13,15] based on maximizing cross-correlation of the measured and re-projected images can correct only for translational misalignments, while the method in [14] relies on the projection of the tube holding the sample for pre-alignment of the angle between the actual rotation axis and the optical axis followed by iterative correction of the translation and tilt angle by cross-correlation. The method in [18] corrects only for translations and uncertainty in the tomographic angle. Both [16,17] correct for translations and rotations, but the algorithm in [16] is designed for structure refinement in the final stages of single-particle reconstruction in electron microscopy and is based on the assumption that a low quality reconstruction and reasonable guesses for orientation parameters are available. In [19], the authors demonstrate a hybrid iterative approach based on applying several image registration algorithms, with the sequence of application dependent upon the particular experiment.

1.1. New approach

With ever increasing achievable resolution in tomography (e.g. nanoscale tomography), experimental misalignments are comparable to the imaging resolution and have a greater impact on the quality and interpretability of reconstructions. Hence, the need for a generic yet robust algorithm that can automatically correct errors due to mechanical instability becomes important. In this paper we present a robust implementation of the projection matching algorithm that aims to correct for full 3D rigid body motions (rotations and translations) of the sample. Current existing methods based on projection matching employ gradient-based optimization for parameter estimation, but use forward difference approximation for the calculation of derivatives with respect to alignment parameters, thereby compromising accuracy and automation. The difference in the sensitivity of the optimization problem to the magnitudes of the errors in rotations and translations, necessitates different step sizes for the different parameters for accurate computation of derivatives. At the same time, the step sizes must also be varied as the resolution of the reconstruction improves with increasing iterations.

In this paper, we exploit a projection matching approach to build an algorithm that corrects for full 3D rigid body motions (rotations and translations) of the sample. We describe a new scheme to calculate the forward projection matrix which allows us to derive analytical expressions for derivatives of the cost function with respect to alignment parameters (rotations and translations). Our method is fully automated in that it does not require pre-alignment or determination of an optimal step-size for computation of derivatives, nor does it rely on exploiting any special

symmetry in the geometry of the experiment. While the analysis and results presented in this paper are for tomography in the parallel-beam setup, our formulation is completely general and can be easily modified for a different experimental geometry, such as cone-beam tomography (CBT).

We demonstrate the robustness of our method to misalignments through a series of simulations on phantom data with increasing degree of misalignments, and establish a limit on the amount of error that can be handled with our approach. Finally, we describe a multi-resolution approach for joint alignment and reconstruction, and demonstrate its effectiveness on two experimental datasets: a biological sample collected at the Advanced Light Source (ALS), and a solid-state battery material collected at the Stanford Synchrotron Radiation Lightsource (SSRL).

2. Methods

2.1. Alignment parameters

We model the motions of the sample/stage as 3D rigid-body transformations consisting of three rotations (α about x-axis, β about y-axis, and ϕ about the z-axis), and three translations (Δx, Δy, and Δz along the x-, y-, and z-axes, respectively, as shown in Fig. 1(a)). The axis along which the incident X-rays travel is called the optical axis, and the axis about which the object is rotated is called the tomographic axis. Here, the the y-axis is the optical axis and the z-axis is the tomographic axis. Since in this work we only consider the parallel-beam setup, under the assumption that the incident beam is perpendicular to the plane of the detector, motions along the optical axis can be ignored. As such there are 5 degrees of freedom (DOF) for each projection, represented as a single vector $\Theta = [\alpha, \beta, \phi, \Delta x, \Delta z]$. The rigid body transformation is defined by a linear affine function that implements rotations and translations applied in an order such that motions along the optical axis do not alter the projections. The action of the affine map T is given as

$$T\mathbf{x} = R^y_\beta R^x_\alpha R^z_\phi \mathbf{x} + \mathbf{t},\tag{1}$$

where $\mathbf{x}$ are points on which the 3D object f is sampled, $\mathbf{t} = [\Delta x, \Delta y, \Delta z]$ is the vector of translations, and R^μ_δ is the matrix for rotation by angle δ about axis μ. Alternatively, instead of applying transformations to the 3D object, we can apply the inverse of the affine map T to points on the source and detector to trace x-rays through the object. Given untransformed pairs of points $\mathbf{p}_s$ and $\mathbf{p}_d$ on the source and detector, respectively, and step size Δs, the ray-tracing path is characterized by the set of points $\mathbf{p}_j$

$$\mathbf{p}_j = T^{-1}\mathbf{p}_s + j\Delta s\hat{\mathbf{r}}\tag{2}$$

with

$$\mathbf{r} = T^{-1}\mathbf{p}_d - T^{-1}\mathbf{p}_s,$$
$$\hat{\mathbf{r}} = \frac{\mathbf{r}}{|\mathbf{p}_d - \mathbf{p}_s|}.$$

Here $\mathbf{r}$ is the ray-vector connecting the points on the source and the detector, $\hat{\mathbf{r}}$ is the unit ray-vector, and we have exploited the fact that our affine map consists of rotations and translations only.

2.2. Optimization problem

The joint alignment and reconstruction of tomographic data is formulated as a nonlinear least-squares minimization problem of the form

$$(f^*, \Theta^*) = \underset{f\in\mathbb{R}^n, \Theta\in[\Theta_{min}, \Theta_{max}]}{\arg\min} \frac{1}{2}||A(\Theta)f - p||^2_2 + \lambda R(f),\tag{3}$$

where f is the vector containing voxel values, Θ is the vector of alignment parameters, A is the forward projection matrix that implements a line-integral for each ray $\hat{\mathbf{r}}$, p is the vector of tomographic measurements, and $R(f)$ is a term enforcing regularization with weight factor λ.

The optimization problem (3) in $\{f, \Theta\}$ is generally difficult to solve due to the nonlinear coupling between the unknown 3D object f and alignment parameters Θ and ill-conditioning due to differences in the scales of f and Θ. The problem is commonly solved by iteratively alternating between two simpler sub-problems [14,16,17]:

(1) Regularized tomographic reconstruction at current estimate of alignment parameters Θ

$$f^k = \arg \min_f \left\{ \frac{1}{2} ||A(\Theta^{k-1})f - p||_2^2 + \lambda R(f) \right\}. \tag{4}$$

(2) Estimation of alignment parameters by projection-matching which minimizes discrepancies between the measured projections and calculated projections from current estimate of the reconstruction f

$$\Theta^k = \arg \min_\Theta \frac{1}{2} ||A(\Theta)f^k - p||_2^2. \tag{5}$$

Splitting the problem in this way makes it possible to use various existing reconstruction techniques to solve the tomography sub-problem, and at the same time independence of alignment parameters for different projections enables parallelization of the projection-matching step.

In our implementation of tomographic reconstruction our regularization term is a sparse prior defined in terms of the total variation (TV), which yields improved reconstructions for noisy and incomplete measurements. The minimization problem is given by

$$f^* = \frac{1}{2} \arg \min_f \left\{ ||A(\Theta)f - p||_2^2 + \lambda ||f|_{\text{TV}} =: g(f, \Theta) + h(f) \right\}. \tag{6}$$

Here the regularization term is the isotropic total variation of f

$$||f||_{\text{TV}} = \sqrt{\left|D_x f\right|^2 + \left|D_y f\right|^2 + \left|D_z f\right|^2}$$

with the $D_i f$ giving the finite difference approximation to the gradient of f. We solve this problem by using the fast iterative shrinkage/thresholding algorithm (FISTA) [20]

$$\begin{aligned} u^{(k)} &= \text{prox}_h \left(f^{k-1} - \tilde{\lambda} \nabla g(f^{k-1}) \right); \quad \tilde{\lambda} = \frac{\lambda}{L_A}; \quad L_A = ||A||_2^2 \\ t^{(k)} &= \frac{1}{2} \left(1 + \sqrt{1 + 4t^{2,(k-1)}} \right); \quad t^{(0)} = 1 \\ f^{(k)} &= u^{(k)} + \frac{t^{(k-1)} - 1}{t^{(k)}} \left(u^{(k)} - u^{(k-1)} \right). \end{aligned} \tag{7}$$

where $\text{prox}_h(\mathbf{x})$ is the proximal mapping of $h : \mathbb{R} \to \mathbb{R}$ given by

$$\text{prox}_h(\mathbf{x}) = \arg \min_{\mathbf{u} \in \mathbb{R}} \left\{ h(\mathbf{u}) + \frac{1}{2} ||\mathbf{u}\text{-}\mathbf{x}||_2^2 \right\} \text{ for any } \mathbf{x} \in \mathbb{R}.$$

Non-negativity of $f^{(k)}$ can be imposed by setting negative values to zero at the end of each FISTA iteration.

2.3. Forward projection

Our forward projector is a generalization of the Joseph's algorithm [21,22], but instead of using the length of intersection of the rays with the object pixels, we use interpolation to compute the contribution of the object pixels to the forward projection (Fig. 1(b)). The action of the forward projector on the 3D object can be written as

$$A(\Theta)f = \sum_j \sum_{\mathbf{x}_g} f(\mathbf{x}_g)k(\mathbf{p}_j - \mathbf{x}_g), \qquad (8)$$

where $k(\mathbf{x})$ is an interpolation kernel, f is sampled over a uniform grid $\mathbf{x}_g$, and the points $\mathbf{p}_j$ are uniformly sampled on the rays passing through the object from the source to the detector. Throughout this work we use trilinear interpolation for which the interpolation kernel is given as

$$k(\mathbf{x}) = k(x)k(y)k(z), \qquad (9)$$

where $\mathbf{x} = (x, y, z)$, and

$$k(x) = \begin{cases} 1 - |x| & \text{if} |x| \in [0, 1] \\ 0 & \text{otherwise.} \end{cases}$$

The derivative of (8) with respect to Θ is given as

$$
\begin{aligned}
\nabla_\Theta A(\Theta)f &= \sum_j \sum_{\mathbf{x}_g} f(\mathbf{x}_g)\nabla_\Theta k(\mathbf{p}_j - \mathbf{x}_g) \\
&= \sum_j \sum_{\mathbf{x}_g} f(\mathbf{x}_g)\frac{\partial \mathbf{p}_j}{\partial \Theta} \cdot \left(\nabla k(\mathbf{p}_j - \mathbf{x}_g)\right)^T.
\end{aligned}
\qquad (10)
$$

Using Eqs. (1) and (2), the derivatives of points $\mathbf{p}_j$ with respect to Θ can be exactly computed. For example, the derivative of point $\mathbf{p}_j$ with respect to the tomographic angle ϕ can be written as

$$\frac{\partial \mathbf{p}_j}{\partial \phi} = \frac{\partial T^{-1}}{\partial \phi}\left(\mathbf{p}_s + j\Delta s \frac{\mathbf{p}_d - \mathbf{p}_s}{|\mathbf{p}_d - \mathbf{p}_s|}\right),$$

where

$$\frac{\partial T^{-1}}{\partial \phi} = \frac{\partial R^z_{-\phi}}{\partial \phi}R^x_{-\alpha}R^y_{-\beta}$$

is a 3×3 matrix. The derivatives with respect to all other parameters can be calculated similarly. Since our interpolation kernel is also differentiable, the gradients in Eq. (10) can be computed exactly. We note that this formalism can be extended to more general and higher order interpolating kernels of the form $k(\mathbf{p}_j, \mathbf{x}_g)$.

The cost function for projection matching is

$$g(\Theta) = \frac{1}{2}||A(\Theta)f - p||^2_2, \qquad (11)$$

and its derivative with respect to the alignment parameters are given by

$$\nabla_\Theta g(\Theta) = (\nabla_\Theta A(\Theta)f)^T \cdot (A(\Theta)f - p). \qquad (12)$$

The optimization of alignment parameters which was solved via quasi-Newton methods (BFGS, L-BFGS-B) [23].

3.   Results

Our results on simulated and experimental data have been obtained using an in-house implementation of the forward and backward projection operators that allow for full 3D rigid body motion. For fast evaluation of the X-ray transform, the ray-tracing was implemented in Fortran. Linear algebra operations for reconstruction were implemented using scipy's sparse matrix package, and quasi-Newton optimization was performed using scipy's optimization library [24].

3.1.   Simulated data

We test our joint alignment and reconstruction algorithm on a phantom of size $128 \times 128 \times 128$ made up of spheres, ellipsoids, and cuboids of random dimensions and centers. We generate noiseless tomographic projections for a parallel beam setup at 90 projection angles ϕ equally spaced between $[0°, 180°]$. To demonstrate the robustness of the algorithm, we present results on four simulated datasets with increasing degree of misalignments as follows:

Dataset 1. In-plane and axial translations uniformly distributed between ±2 pixels (1.5% linear dimension), α and β normally distributed with $\sigma = 0.25°$ (maximum offset = 0.6°), and $\Delta\phi$ uniformly distributed between ±0.25°.

Dataset 2. In-plane and axial translations uniformly distributed between ±8 pixels (6.25% linear dimension), α and β normally distributed with $\sigma = 1.5°$ (maximum offset = 2.7°), and no perturbation in the tomographic angle ϕ.

Dataset 3. In-plane and axial translations uniformly distributed between ±16 pixels (12.5% linear dimension), α and β normally distributed with $\sigma = 3.0°$ (maximum offset = 7.5°), and no perturbation in the tomographic angle ϕ.

Dataset 4. In-plane and axial translations uniformly distributed between ±40 pixels (31.2% linear dimension), α and β normally distributed with $\sigma = 4.0°$ (maximum offset = 13.8°), and no perturbation in the tomographic angle ϕ.

Since the tomographic angle is calibrated to high precision in most experimental setups, we do not perturb this parameter in simulations with large angular and translational misalignments. In Table 1 we also show results for the same parameters as dataset 1, but without jitter in the tomographic angle (dataset 1*). In appendix A and B we show results for simulated datasets with only translational and only rotational misalignments, respectively.

Table 1. Alignment errors for simulated datasets in terms of L1-norm and maximum value of the difference between the ground truth and recovered parameters.

| (max., mean)	$\left|\Delta x_{gt} - \Delta x\right|$ (pix.)	$\left|\Delta z_{gt} - \Delta z\right|$ (pix.)	$\left|\alpha_{gt} - \alpha\right|$ (deg.)	$\left|\beta_{gt} - \beta\right|$ (deg.)	$\left|\phi_{gt} - \phi\right|$ (deg.)
Dataset 1	0.08, 0.04	0.003, 0.002	0.006, 0.002	0.006, 0.002	0.02, 0.008
Dataset 1*	0.03, 0.01	0.002, 0.0006	0.004, 0.002	0.005, 0.002	––
Dataset 2	0.11, 0.06	0.01, 0.005	0.02, 0.004	0.08, 0.006	––
Dataset 3	0.35, 0.12	0.24, 0.08	0.09, 0.04	0.08, 0.03	––

The joint alignment and reconstruction scheme was run for 30 - 50 outer iterations, and within each iteration we alternated between tomographic reconstruction and alignment. The initial guesses for f and Θ were set to zero. For tomographic reconstruction, we use λ=1 for dataset 1, and $\lambda = 10$ for all other datasets. In general, it is possible to continuously vary the regularization parameter during the iterative scheme, starting with a high value of λ and gradually

reducing it as the alignment parameters converge. At every outer iteration, the reconstruction is terminated either when the maximum number of reconstruction iterations is reached (fixed at 250) or when semi-convergence is reached ($r^k > r^{k-1}$ where $r^k = ||Af^k - p||_2$). For optimization of alignment parameters, we use the quasi-Newton L-BFGS method with bound constraints on all alignment parameters. The alignment iteration for individual projections is terminated if the relative reduction in cost is less than 10^{-7} or the maximum value of the projected gradient is less than 10^{-5}.

We show the results of our algorithms for simulated datasets 1, 2, and 3 in Figs. 2, 3, and 4, respectively. The first two rows show plots of the ground truth (blue circles) and fitted (orange triangles) alignment parameters, and the mean-squared errors (MSE) of the projections (green solid) and reconstruction (red dashed) calculated as $\frac{||x_{\text{rec}} - x_{\text{gt}}||_2^2}{||x_{\text{gt}}||_2^2}$. The MSE for projections (labelled as data error in plots) is computed between the measured data and reprojections from the current estimate of the reconstruction. The third and fourth rows show orthogonal slices through the unaligned and aligned reconstructions and the central measured and calculated sinogram, respectively. The severity of the misalignments for the different datasets is evident from the degree to which the unaligned reconstruction is blurred. For example, for dataset 1 with minimal perturbations, the features in the phantom are easily visible in the unaligned reconstruction, whereas for dataset 3 with relatively large perturbations, the unaligned reconstruction is rather featureless. For all three cases, we observe that the alignment parameters are recovered with sub-pixel accuracy in translations and up to 0.05 degrees accuracy in rotations, as seen from Table 1. An observation from the MSE plots is that the error decreases rapidly over the first 20 iterations and plateaus thereafter, showing that once a sufficient number of projections are aligned correctly, there is not a significant effect on the final reconstruction. It is worth noting here that the projections are invariant to a global affine transformation of the 3D object due to motions such as a constant shift of the center-of-rotation (perpendicular to the tomographic axis), constant axial translation (along the tomographic axis), and constant tilt of the tomographic axis [25]. For the simulated datasets, these global shifts are determined using an extension of the orthogonal Procrustes analysis [26] which yields an overall global transformation that is applied to the recovered alignment parameters before computing alignment and reconstruction errors.
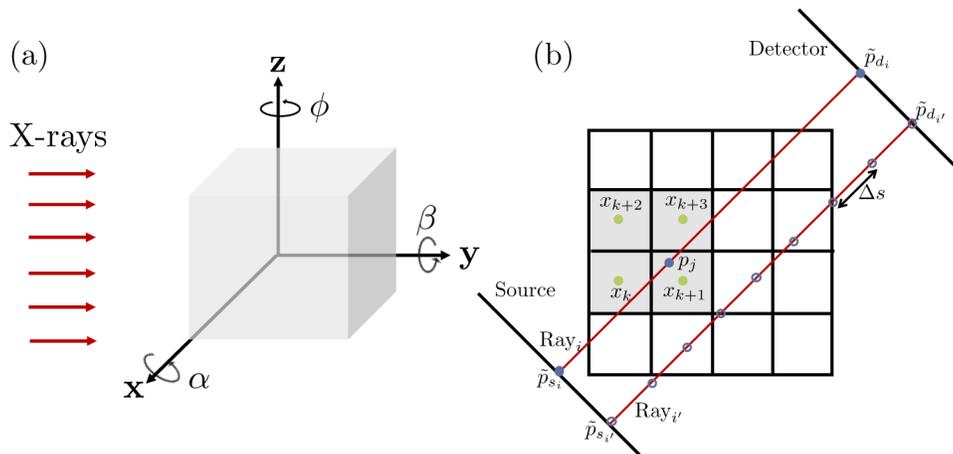

Fig. 1. (a) Setup for parallel beam tomography with 5 degrees of freedom modeled as rigid body transformations. (b) Ray-tracing through a 2D object: Source-detector pair $(\tilde{p}_{s_i}, \tilde{p}_{d_i})$ represent affine transformed points on the source and detector for i^{th} ray. The object is sampled over a uniform grid $\mathbf{x}_g$ and linear interpolation is used to compute the pixel intensity at points $\mathbf{p}_j$ along the rays.
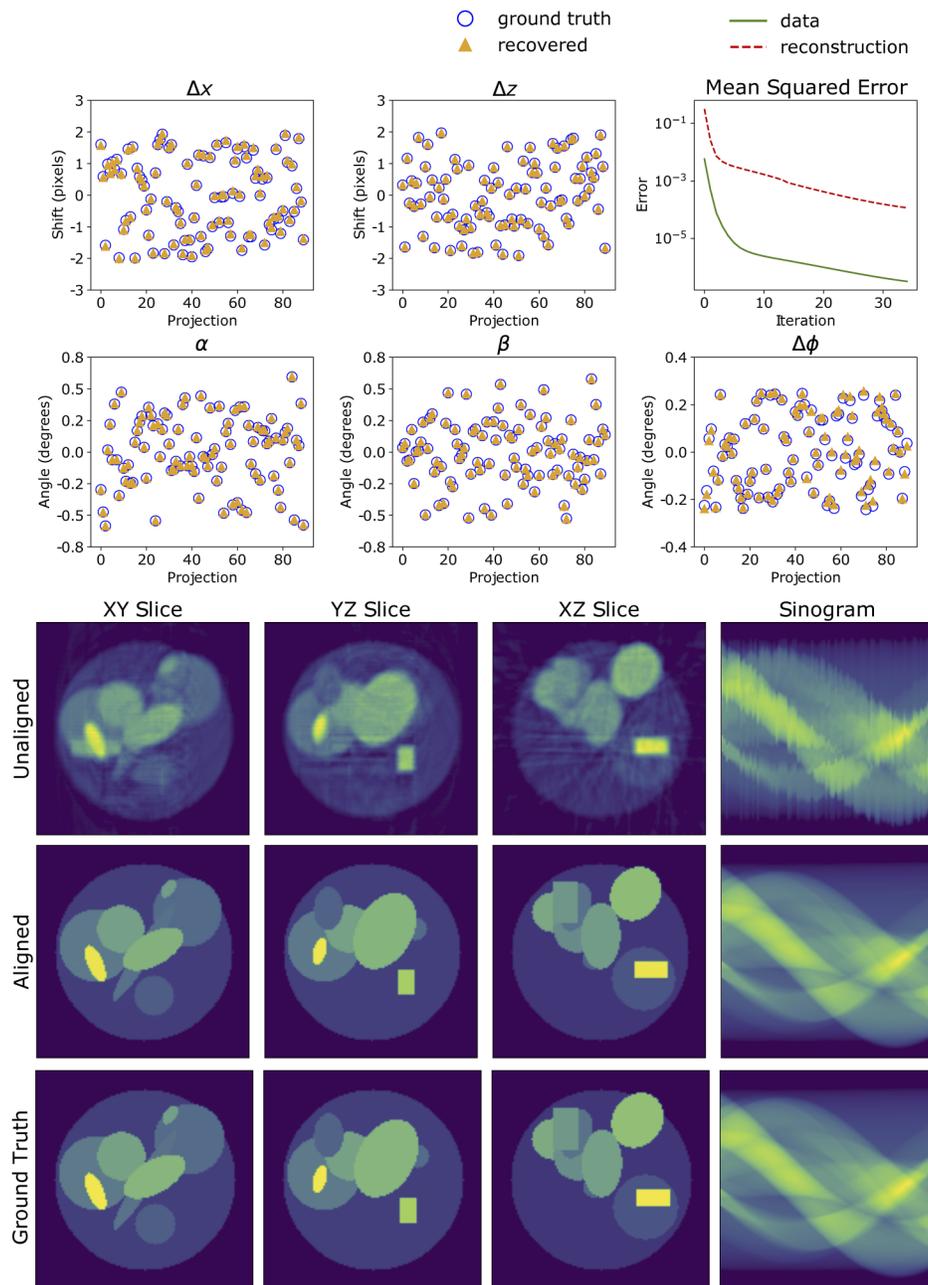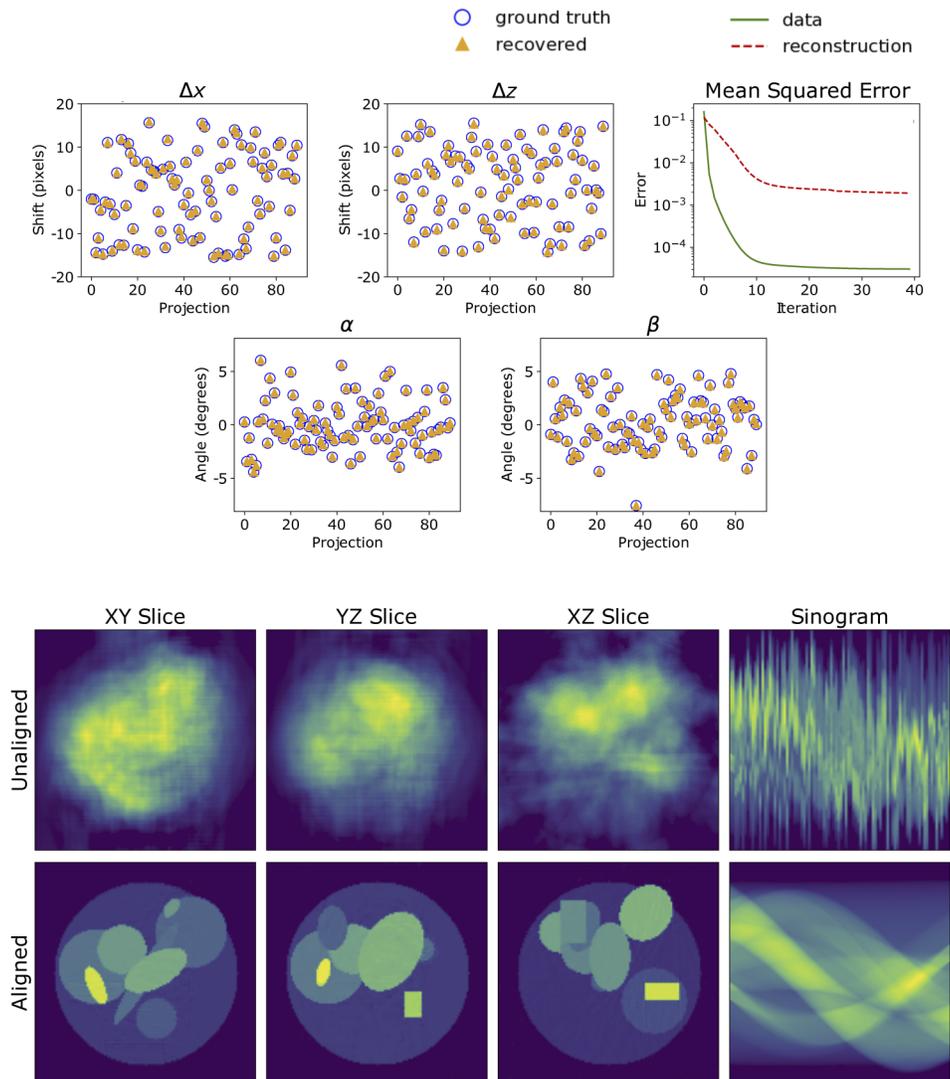
Fig. 2. Recovered parameters and reconstruction for dataset 1 with smallest misalignments corresponding to a maximum of 2 pixels (1.5%) offset in translations and 0.6° degrees in rotations. Ground truth and recovered parameters are displayed as empty blue circles and solid orange triangles, respectively.

Through a series of simulations we find that the magnitude of the translation error has a greater impact on parameter recovery. Keeping the magnitude of translation error fixed at 12.5%, we varied the angular error by $\sigma = 3.0, 3.5, 4.0$ in three separate simulations and found that we were able to recover the angles to within 0.1° accuracy and the translations to within 0.1 (0.25), 0.1 (0.3) and 0.2 (0.5) pixels accuracy, respectively. Here the values in brackets denote the maximum
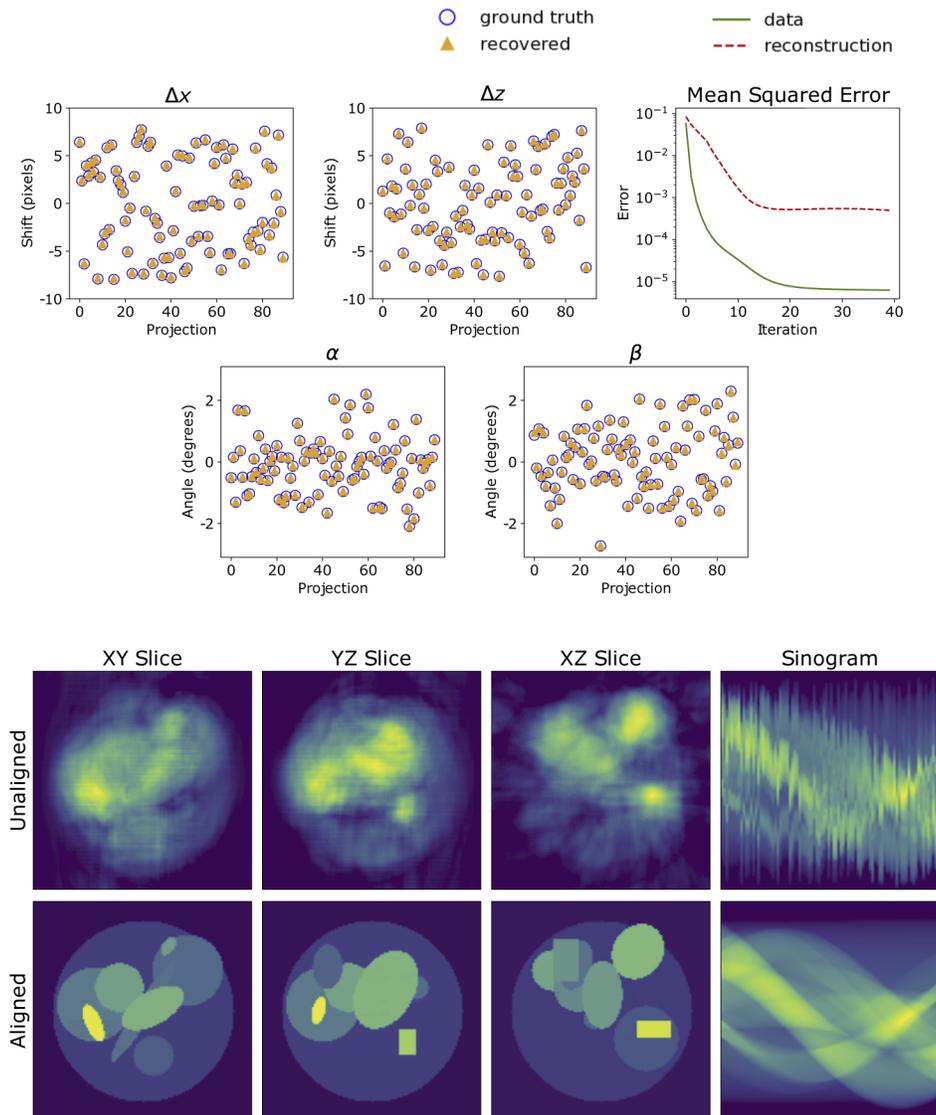
Fig. 3. Recovered parameters and reconstruction for simulated dataset 2 with moderate misalignments corresponding to a maximum of 8 pixels (6.25%) offset in translations and 2.7° degrees in rotations. Ground truth and recovered parameters are displayed as empty blue circles and solid orange triangles, respectively.

difference between ground truth and found parameters. On the other hand, keeping the angular error fixed with $\sigma = 3.0$ we varied the translation error by 12.5%, 20%, and 31.2% and found that the angular parameters are recovered to within 0.1° (~ 0.8°), while the translation parameters are found to within 0.1 (0.25), 0.4 (1.0), and 1.25 (3.5) pixels, respectively. This shows that the parameters are recovered well for moderate translation misalignment, even for a high angular error. Finally, we note that we reach the breaking point for our alignment algorithm for dataset 4 with translation errors as large as 40 pixels (31.2% of linear dimension) and rotation errors normally distributed with $\sigma = 4.0$ (maximum error ~ 14°). In this extreme case, and in the absence of pre-alignment or a low resolution prior, we were unable to reach convergence for

Fig. 4. Recovered parameters and reconstruction for simulated dataset 3 with severe misalignments corresponding to a maximum of 16 pixels (12.5%) offset in translations and 7.5° degrees in rotations. Ground truth and recovered parameters are displayed as empty blue circles and solid orange triangles, respectively.

enough projections so as to obtain the correct reconstruction, suggesting that there is an upper limit to the amount of error that our algorithm can tolerate.

Our code is parallelized using the Message Passing Interface (MPI) standard. Simulations were run with 30 MPI ranks on 3 nodes with a 2.3 GHz Intel Xeon "Haswell" processor. Both the reconstruction and alignment were parallelized over projections, resulting in every MPI rank handling 3 projections (each dataset consists of 90 projections). On average, a single joint alignment-reconstruction iteration took less than 5 minutes.
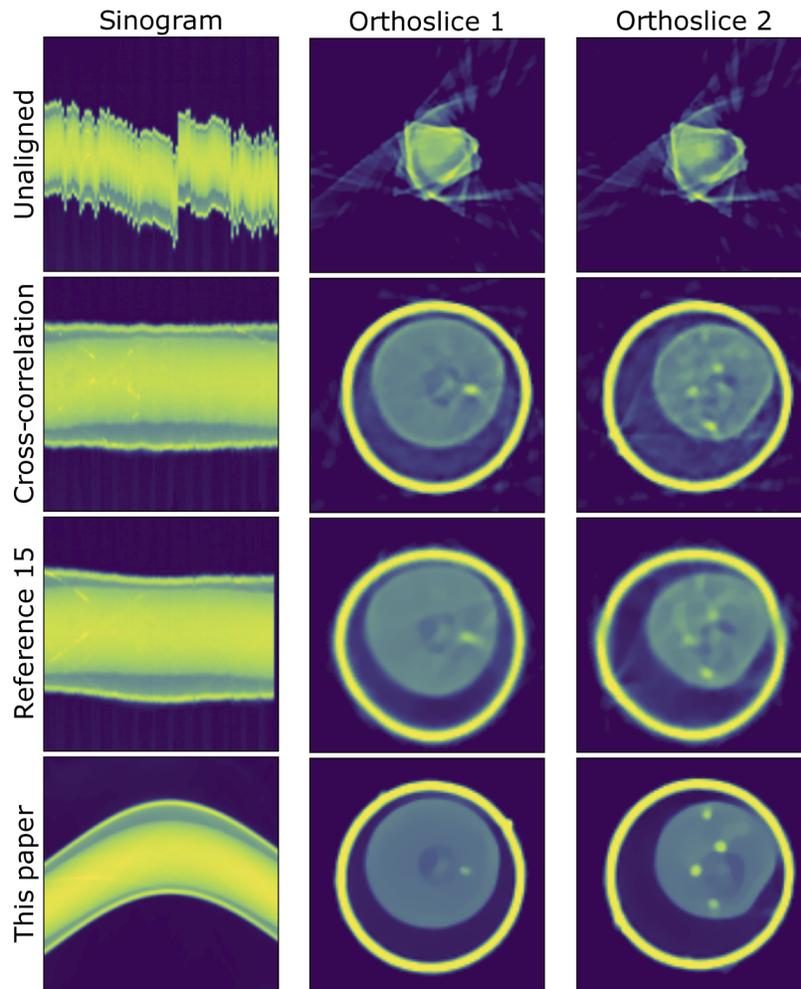
Fig. 5. Comparison of sinogram and orthoslices through the reconstruction for the ALS biological dataset for unaligned data, data aligned with cross-correlation, the iterative reprojection algorithm described in [15] and the multi-resolution alignment algorithm proposed in this paper. Note the difference in the sinogram for cross-correlation and 3D alignment due to an offset in the center-of-rotation.

3.2. Experimental data

To demonstrate the full potential of our method, we now present results on alignment of two experimental datasets: (1) biological cell in a cylinder collected at the soft x-ray tomography beamline at the ALS [27], and (2) XANES data (single energy) of an NMC battery cathode particle collected at the SSRL and publicly available in TomoBank [28] (ID 00089). The first row of Figs. 5 and 7 shows the central sinogram and slices through the unaligned reconstruction for the two datasets. For both these data we compare the alignment by cross-correlation, iterative reprojection method detailed in [15] and the method proposed in this paper. However we note that [15] uses a different forward operator and regularization scheme, which may impact the quality of the final reconstruction.

For the experimental data, we employ a multi-resolution [11,18] approach to reduce the computational time and memory requirements by going from a coarse to a fine sampling of the

projections. Lowering the resolution results in smoothing of the projection data, which also serves as a regularization of the optimization problem, thereby reducing the low frequency components of the alignment error. In our observation the translation parameters are well determined at relatively coarse resolutions, while the determination of the angular parameters improves at fine resolutions when smaller features in the projections can be resolved. For both the experimental datasets, we align only in-plane and axial translations at the coarsest resolution.

We first show results for the biological dataset. The measured data consists of a full rotation series with 93 projections of size 1024×1024. At the coarsest resolution, the images were binned to size 64×64, and alignment and reconstruction was done up to an image size of 256×256. In Fig. 5 we show the central sinogram and orthoslices through the reconstruction before alignment (top row), after alignment using the cross-correlation method (second row), the algorithm in [15] (third row), and with the method proposed in this paper (fourth row). The recovered alignment parameters are shown in Fig. 6. Because of the cylindrical nature of the experimental setup, we expect the capillary tube-wall to be circular once the data is well-aligned, with misalignments manifesting in the form of distorted or discontinuous circle. As seen in Fig. 5 the reconstruction with cross-correlation alignment and the alignment method in [15] shows a non-circular tube-wall as well as blurred features inside the cell, while the reconstruction with our proposed method yields a nearly circular tube and clearly visible sub-cellular organelles. The improvement in the quality of reconstruction obtained by our proposed method compared to that in [15] shows that in this particular case alignment of both rotations and translations is important.
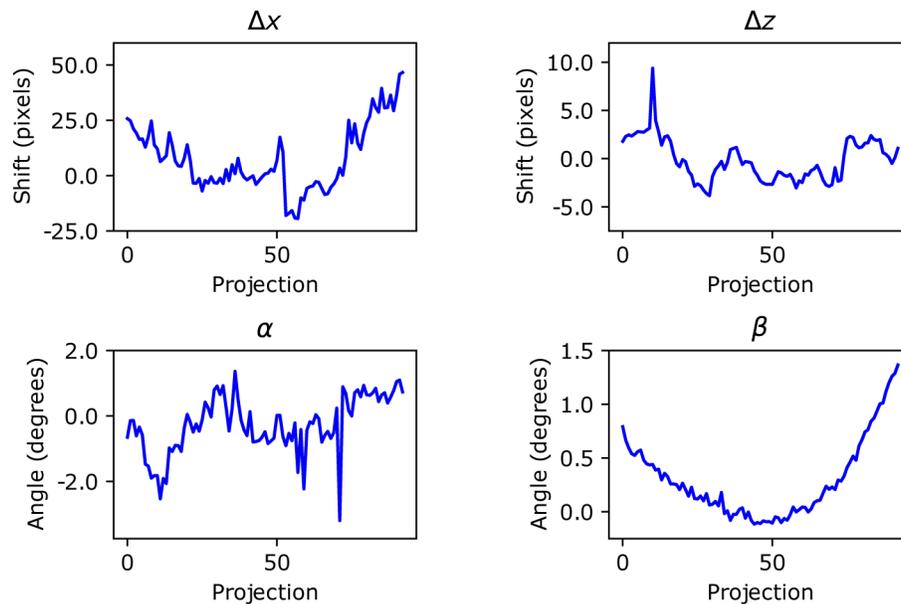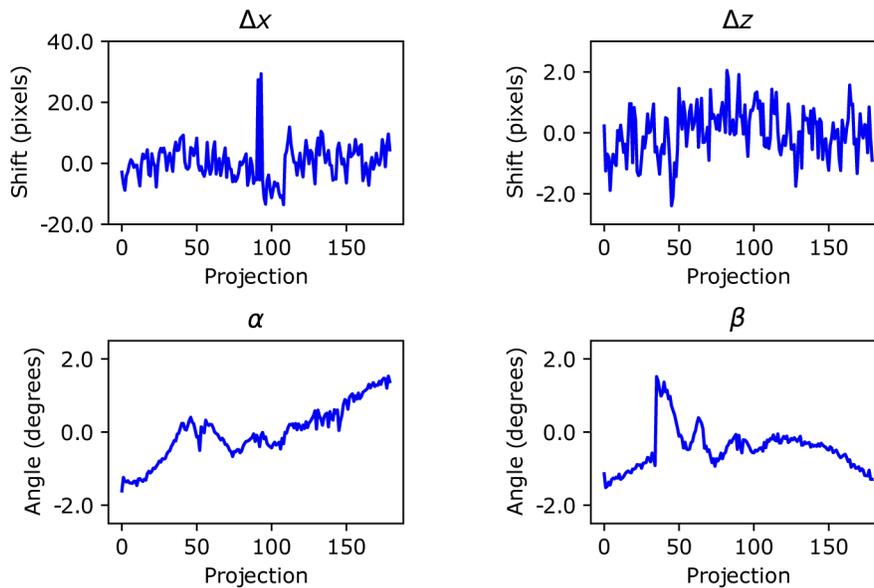

Fig. 6. Recovered alignment parameters for biological dataset collected at the ALS for projections of size 256×256.

Next, we show results for the XANES dataset collected at the SSRL. This dataset consisted of a full rotation series with 180 projections of size 1024×1024. The projections were first cropped to size 640×640, and then sequentially aligned and reconstructed starting with the coarsest resolution of image size 80×80 and the final resolution of image size 320×320. In Fig. 7 we show the central sinogram and orthogonal slices through the reconstruction before alignment (top row), after alignment using the cross-correlation method (second row), the algorithm in [15] (third row), and with the method proposed in this paper (fourth row). The corresponding recovered

alignment parameters are shown in Fig. 8. A qualitative comparison of the reconstruction slices shows that while both our method and the method in [15] yield reconstructions with sharper boundaries as compared to the reconstruction with cross-correlation alignment, our method produces a reconstruction with better contrast and features.
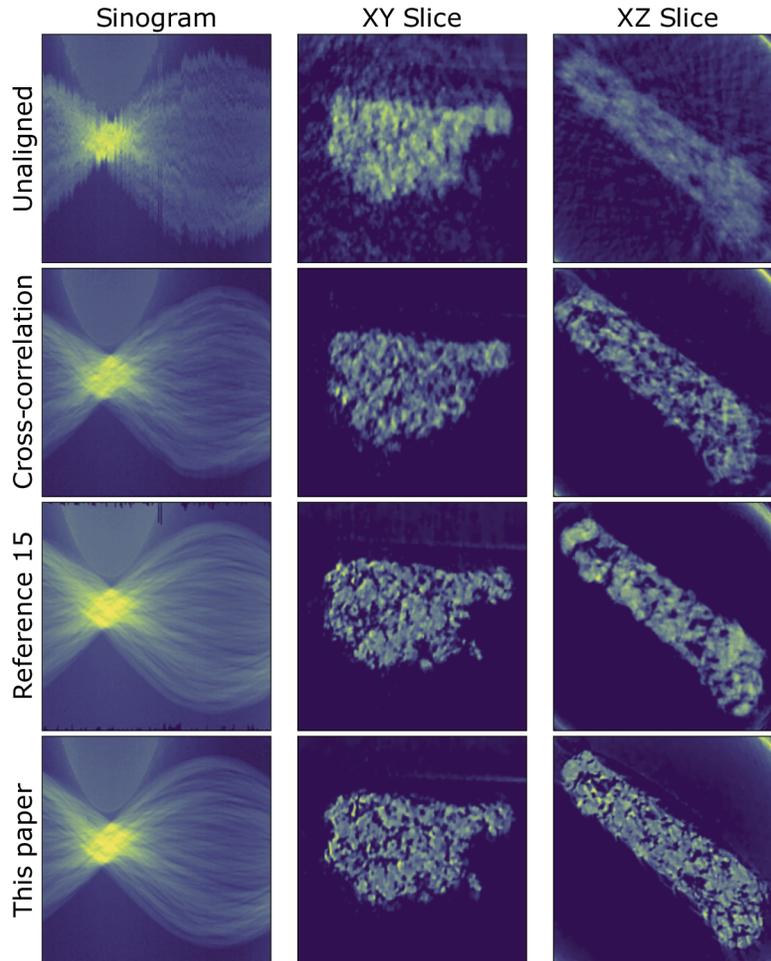
Fig. 7. Comparison of sinogram and slices through the reconstruction for the SSRL XANES dataset for unaligned data, data aligned with cross-correlation, the iterative reprojection algorithm described in [15] and the multi-resolution alignment algorithm proposed in this paper.

Fig. 8. Recovered alignment parameters for XANES dataset collected at the SSRL for projections of size 320×320.

4. Conclusions and outlook

The results presented here show that our proposed joint iterative reconstruction and 3D alignment algorithm is able to recover accurate rigid body motions that the sample/stage may undergo during an x-ray tomography experiment. We have described the details of the forward projection operator that takes into account full 3D rigid motions. The analytic computation of derivatives with respect to alignment parameters eliminates the need to choose a step size for calculating the Jacobian matrix using the finite difference method as proposed in [17,18]. Results based on simulations as well as experimental data show that the algorithm performs well even when the misalignments are large. In future work, we aim to optimize the convergence and computational efficiency of the algorithm through a GPU implementation [29] and use of higher order interpolation schemes for the projection operator.

Due to the non-convexity of the cost function in (3), the determination of the global minimum of the problem is not guaranteed, which is a well known general limitation of projection matching algorithms. The multi-resolution approach proposed here and in other work [11,18] has been shown to be effective in avoiding local minima, as evident from our results on the experimental data. One possible route to avoiding such local minima is to use global optimization methods such as simulated annealing and differential evolution, but only at coarse resolutions due to their high computational cost. However, this may not facilitate a convergence to the global minimum for the rotations. A better approach would be to employ more efficient hybrid global and local optimization schemes such as [30] for a few iterations at different levels of the resolutions pyramid to guarantee fast convergence to the global minimum.

An additional key point is that another source of artifacts in tomographic reconstruction is non-rigid deformation processes as a result of time-evolution in dynamic samples and damage induced in radiation sensitive samples. A common approach to model sample evolution is based on the use of deformation vector fields computed from volumes reconstructed from two independent sets of projections from a full rotation series [31–36]. While some of these methods require a prior knowledge of either the nature of the displacement or a template sample

reconstruction from undeformed projections, others are based on a joint optimization framework with a self-consistent method to model continuous deformation of the sample. Although non-rigid deformations lead to significant loss in the quality and resolution of reconstructions, in this work we only address the inconsistencies in projection measurements due to rigid-body motions, and the non-rigid motions will be the subject of a future study.

Appendix A. Effect of only translation misalignment

Figure 9 shows results for simulated dataset with only translation misalignments uniformly distributed between ±40 pixels (31.25% linear dimension). We are able to recover the parameters to within 0.1 pixels accuracy.
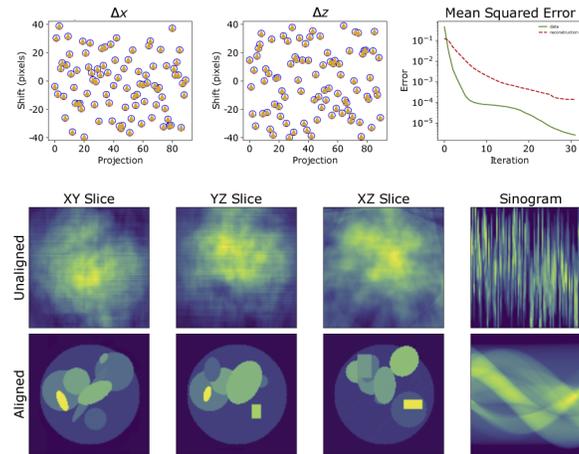
Fig. 9. Recovered parameters and reconstruction for simulated dataset with only translation misalignments uniformly distributed between ±40 pixels (31.25% linear dimension). Ground truth and recovered parameters are displayed as empty blue circles and solid orange triangles, respectively.

Appendix B. Effect of only rotational misalignment

Figure 10 shows results for simulated dataset with only rotational misalignments normally distributed with $\sigma = 4.0°$ (maximum offset = 14.0°). We are able to recover the parameters to within 0.05° accuracy.

Appendix C. Effect of correcting for translations only

Figure 11 shows results for accounting for only translation jitter in a simulated dataset with translation misalignments uniformly distributed between ±16 pixels (6.25% linear dimension) and rotational misalignments normally distributed with $\sigma = 1.5°$ (maximum offset = 2.7°). This corresponds to dataset 2 in the main text.

Appendix D. Fourier shell correlation

Figure 12 shows the Fourier shell correlation (FSC) of the reconstructed phantom with the ground truth for the three simulated datasets. The FSC is given as

$$FSC(q) = \frac{\sum_{q_i \in q} F_1(q_i) \cdot F_2^*(q_i)}{\sqrt{\sum_{q_i \in q} |F_1(q_i)|^2 \cdot \sum_{q_i \in q} |F_2(q_i)|^2}}, \tag{13}$$

where F_1 is the Fourier transform of the ground truth volume and F_2^* is the Fourier transform of the reconstructed volume. For all three datasets the FSC is better than 0.9 to full resolution.

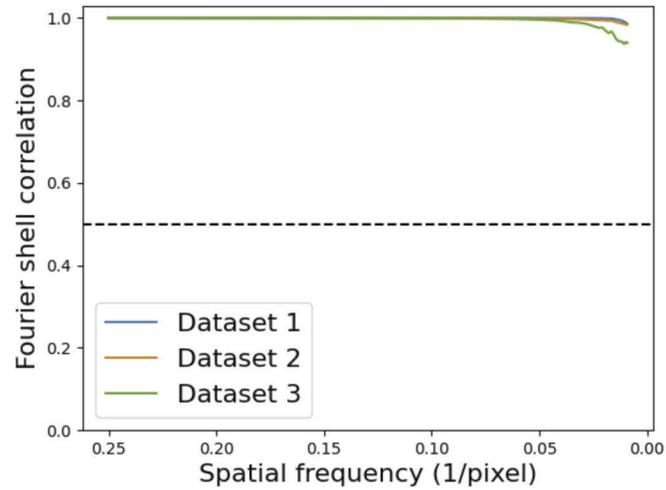## Appendix E. Non-central sinogram slices for simulated phantom

Figure 13 shows non-central unaligned and aligned sinogram slices for the three simulated datasets.
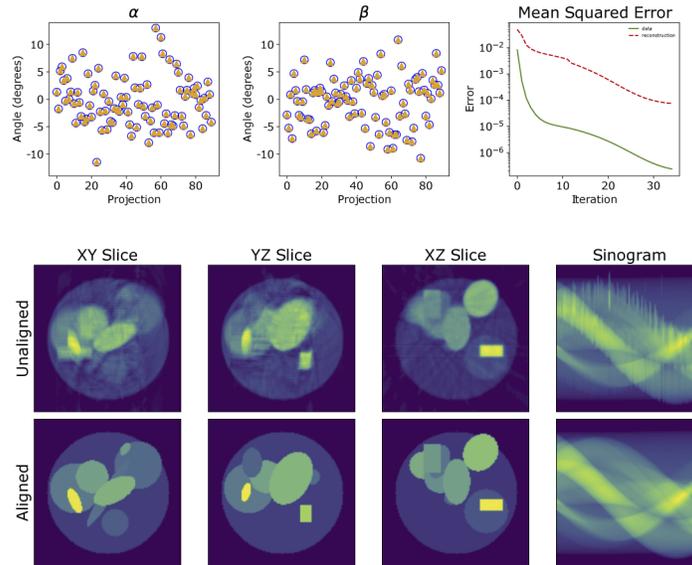

Fig. 10. Recovered parameters and reconstruction for simulated dataset with only rotational misalignments normally distributed with $\sigma = 4.0°$ (maximum offset = 14.0°). Ground truth and recovered parameters are displayed as empty blue circles and solid orange triangles, respectively.
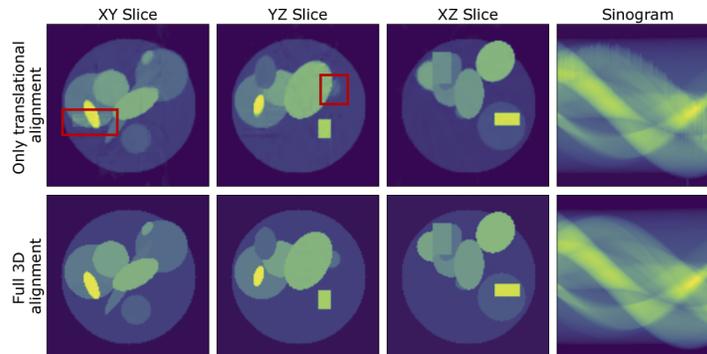
Fig. 11. Comparison of reconstruction and corrected sinogram for dataset 2 (top) accounting for only translation misalignments, and (2) accounting for translation and rotational misalignments. Red boxes in the top row show reconstruction artifacts.

Fig. 12. Fourier shell correlation of the reconstructed volume with the ground truth for simulated dataset 1 (blue), dataset 2 (orange), and dataset 3 (green).
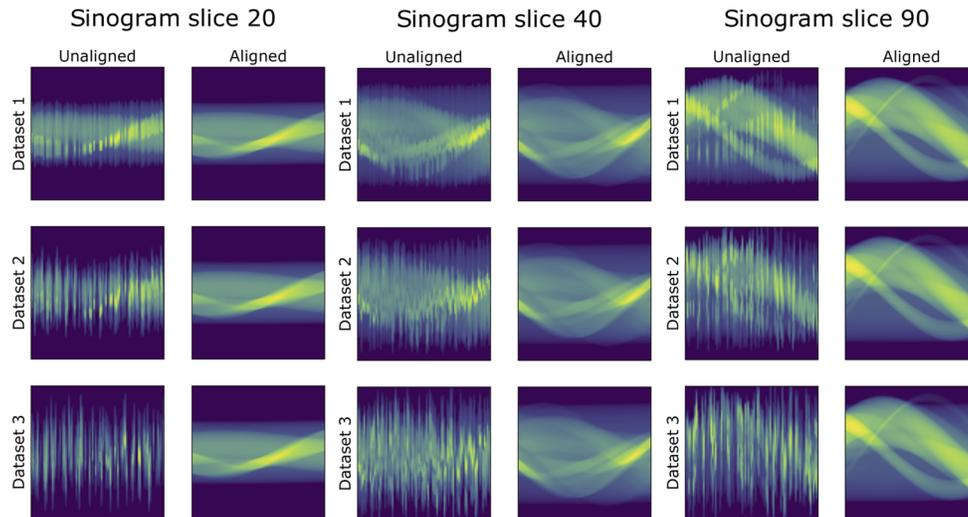
Fig. 13. Unaligned and aligned non-central sinogram slices for the three simulated phantom datasets.

Disclosures. The authors declare no conflicts of interest.

Data availability. Code for 3-D rigid body alignment and reconstruction, and code for generating phantom data as described in this paper is available in Ref. [37]. Biological dataset collected at the ALS is available upon request. XANES dataset is available in tomobank [28] ID 00089.

References

1. C. A. Larabell and M. A. L. Gros, "X-ray tomography generates 3-D reconstructions of the yeast, *Saccharomyces cerevisiae*, at 60-nm resolution," Mol. Biol. Cell **15**(3), 957–962 (2004).
2. R. Mokso, P. Cloetens, E. Maire, W. Ludwig, and J. Y. Buffière, "Nanoscale zoom tomography with hard x rays using Kirkpatrick-Baez optics," Appl. Phys. Lett. **90**(14), 144104 (2007).
3. H. Jiang, C. Song, C. C. Chen, R. Xu, K. S. Raines, B. P. Fahimian, C. H. Lu, T. K. Lee, A. Nakashima, J. Urano, T. Ishikawa, F. Tamanoi, and J. Miao, "Quantitative 3D imaging of whole, unstained cells by using x-ray diffraction microscopy," Proc. Natl. Acad. Sci. USA **107**(25), 11234–11239 (2010).
4. D. E. Olins, A. L. Olins, H. A. Levy, R. C. Durfee, S. M. Margle, E. P. Tinnel, and S. D. Dover, "Electron microscope tomography: transcription in three dimensions," Science **220**(4596), 498–500 (1983).
5. M. Cao, A. Takaoka, H. B. Zhang, and R. Nishi, "An automatic method of detecting and tracking fiducial markers for alignment in electron tomography," J. Electron Microsc. **60**(1), 39–46 (2011).
6. D. N. Mastronarde and S. R. Held, "Automated tilt series alignment and tomographic reconstruction," J. Struct. Biol. **197**(2), 102–113 (2017).
7. W. Hoppe, "Zur elektronenmikroskopisch dreidimensionalen rekonstruktion eines objektes," Naturwissenschaften **61**(12), 534–536 (1974).
8. R. Gluckenberger, "Determination of a common origin in the micrographs of tilt series in three-dimensional electron microscopy," Ultramicroscopy **9**(1-2), 167–173 (1982).
9. J. Frank and B. F. McEwen, *Electron tomography* (Springer, 1992), chap. Alignment by cross-correlation, pp. 205–2013.
10. M. Guizar-Sicairos, A. Diaz, M. Holler, M. S. Lucas, A. Menzel, R. A. Wepf, and O. Bunk, "Phase tomography from x-ray coherent diffractive imaging projections," Opt. Express **19**(22), 21345–21357 (2011).
11. J. Dengler, "A multi-resolution approach to the 3D reconstruction from an electron microscope tilt series solving the alignment problem without gold particles," Ultramicroscopy **30**(3), 337–348 (1989).
12. Y. Liu, P. A. Penczek, B. F. McEwen, and J. Frank, "A marker-free alignment method for electron tomography," Ultramicroscopy **58**(3-4), 393–402 (1995).
13. H. Winkler and K. A. Taylor, "Accurate marker-free alignment with simultaneous geometry determination and reconstruction of tile series in electron tomography," Ultramicroscopy **106**(3), 240–254 (2006).
14. D. Y. Parkinson, C. Knoechel, C. Yang, C. E. Larabell, and M. A. L. Gros, "Automatic alignment and reconstruction of images for soft x-ray tomography," J. Struct. Biol. **177**(2), 259–266 (2012).
15. D. Gürsoy, Y. P. Hong, K. He, K. Hujsak, S. Yoo, S. Chen, Y. Li, M. Ge, L. M. Miller, Y. S. Chu, V. D. Andrade, K. He, O. Cossairt, A. K. Katsaggelos, and C. Jacobsen, "Rapid alignment of nanotomography data using joint iterative reconstruction and reprojection," Sci. Rep. **7**(1), 11818 (2017).
16. C. Yang, E. Ng, and P. A. Penczek, "Unified 3-D structure and projection orientation refinement using quasi-Newton algorithm," J. Struct. Biol. **149**(1), 53–64 (2005).
17. T. Ramos, J. S. Jorgensen, and J. W. Andreasen, "Automated angular and translational tomographic alignment and application to phase-contrast imaging," J. Opt. Soc. Am. A **34**(10), 1830–1843 (2017).
18. F. Bleichrodt and K. J. Batenburg, "Automatic optimization of alignment parameters for tomography datasets," *Proceedings of 18th Scandinavian Conference on Image Analysis* **7944**, 489–500 (2013).
19. H. Yu, S. Xia, C. Wei, Y. Mao, D. Larsson, X. Xiao, P. Pianetta, Y.-S. Yu, and Y. Liu, "Automatic projection image registration for nanoscale X-ray tomographic reconstruction," J. Synchrotron Radiat. **25**(6), 1819–1826 (2018).
20. A. Beck and M. Teboulle, "A fast iterative shrinkage-thresholding algorithm for linear inverse problems," SIAM J. Imaging Sci. **2**(1), 183–202 (2009).
21. P. M. Joseph, "An improved algorithm for reprojecting rays through pixel images," IEEE Trans. Med. Imaging **1**(3), 192–196 (1982).
22. J. Dittman and R. Hanke, "Simple and efficient raycasting on modern GPU's read-and-write memory for fast forward projections in iterative CBCT reconstruction," in *The 14th International Meeting on Fully Three-Dimensional Image Reconstruction in Radiology and Nuclear Medicine*, (2017), pp. 781–784.
23. J. Nocedal and S. Wright, *Numerical Optimization* (Springer, 2006).
24. P. Virtanen, R. Gommers, T. E. Oliphant, M. Haberland, T. Reddy, D. Cournapeau, E. Burovski, P. Peterson, W. Weckesser, J. Bright, S. J. van der Walt, M. Brett, J. Wilson, K. J. Millman, N. Mayorov, A. R. J. Nelson, E. Jones, R. Kern, E. Larson, C. J. Carey, I. Polat, Y. Feng, E. W. Moore, J. VanderPlas, D. Laxalde, J. Perktold, R. Cimrman, I.

Henriksen, E. A. Quintero, C. R. Harris, A. M. Archibald, A. H. Ribeiro, F. Pedregosa, P. van Mulbregt, and SciPy 1.0 Contributors, "SciPy 1.0: Fundamental Algorithms for Scientific Computing in Python," Nat. Methods **17**(3), 261–272 (2020).

25. S. Basu and Y. Bresler, "Uniqueness of tomography with unknown view angles," IEEE Trans. on Image Process. **9**(6), 1094–1106 (2000).

26. J. L. Awange, K.-H. Bae, and S. J. Claessens, "Procrustean solution of the 9-parameter transformation problem," Earth Planet Sp. **60**(6), 529–537 (2008).

27. G. McDermott, M. A. L. Gros, C. G. Knoechel, M. Uchida, and C. A. Larabell, "Soft X-ray tomography and cryogenic light microscopy: the cool combination in cellular imaging," Trends Cell Biol. **19**(11), 587–595 (2009).

28. F. D. Carlo, D. Gürsoy, D. J. Ching, K. J. Batenburg, W. Ludwig, L. Mancini, F. Marone, R. Mokso, D. M. Pelt, J. Sijbers, and M. Rivers, "Tomobank: a tomographic data repository for computational x-ray science," Meas. Sci. Technol. **29**(3), 034004 (2018).

29. D. Kumar, D. Y. Parkinson, and J. A. Sethian, "GPU accelerated iterative tomographic reconstructions," (*in preparation*).

30. M. Noack and S. W. Funke, "Hybrid genetic deflated newton method for global optimisation," J. Comput. Appl. Math. **325**, 97–112 (2017).

31. B. K. Bay, T. S. Smith, D. P. Fyhrie, and M. Saad, "Digital volume correlations: Three-dimensional strain mapping using x-ray tomography," Exp. Mech. **39**(3), 217–226 (1999).

32. G. H. Chen, P. Thériault-Lauzier, J. Tang, B. Nett, S. Leng, J. Zambelli, Z. Qi, N. Bevins, A. Raval, S. Reeder, and H. Rowley, "Time-resolved interventional cardiac C-arm cone-beam CT: An application of the PICCS algorithm," IEEE Trans. Med. Imaging **31**(4), 907–923 (2012).

33. H. Leclerc, S. Roux, and F. Hild, "Projection savings in ct-based digital volume correlation," Exp. Mech. **55**(1), 275–287 (2015).

34. T. D. Schryver, M. Dierick, M. Heyndrickx, J. V. Strappen, M. A. Boone, L. V. Hoorebeke, and M. N. Boone, "Motion compensated micro-CT reconstruction for in-situ analysis of dynamic processes," Sci. Rep. **8**(1), 7655 (2018).

35. M. Odstrcil, M. Holler, J. Raabe, A. Sepe, X. Sheng, S. Vignolini, C. Schroer, and M. Guizar-Sicaros, "Ab initio nonrigid X-ray nanotomography," Nat. Commun. **10**(1), 2600 (2019).

36. V. Nikitin, V. D. Andrade, A. Slyamov, B. J. Gould, Y. Zhang, V. Sampathkumar, N. Kasthuri, and D. Gürsoy, "Distributed optimization for non-rigid nano-tomography," IEEE Trans. Comput. Imaging **7**, 272–287 (2021).

37. K. Pande, J. J. Donatelli, D. Y. Parkinson, H. Yan, and J. A. Sethian, "Rigid body alignment for x-ray tomography data," Github (2021), https://github.com/pandekan/tomography_alignment.